

# Absorption and Emission Spectra of a Flexible Dye in Solution: A Computational Time-Dependent Approach

Nicola De Mitri,<sup>\*,†</sup> Susanna Monti,<sup>†,‡</sup> Giacomo Prampolini,<sup>§</sup> and Vincenzo Barone<sup>†</sup>

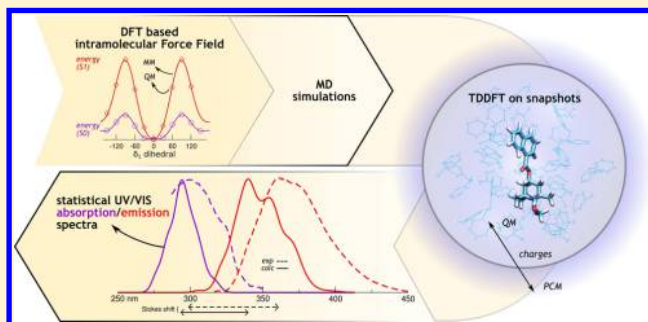
<sup>†</sup>Scuola Normale Superiore, piazza dei Cavalieri 7, I-56126 Pisa, Italy

<sup>‡</sup>Istituto di Chimica dei Composti OrganoMetallici (ICCOM-CNR), Area della Ricerca, via G. Moruzzi 1, I-56124 Pisa, Italy

<sup>§</sup>Istituto per i Processi Chimico-Fisici (IPCF-CNR), Area della Ricerca, via G. Moruzzi 1, I-56124 Pisa, Italy

## Supporting Information

**ABSTRACT:** The spectroscopic properties of the organic chromophore 4-naphthoxy-1-methoxy-2,2,6,6-tetramethylpiperidine (NfO-TEMPO-Me) in toluene solution are explored through an integrated computational strategy combining a classical dynamic sampling with a quantum mechanical description within the framework of the time-dependent density functional theory (TDDFT) approach. The atomistic simulations are based on an accurately parametrized force field, specifically designed to represent the conformational behavior of the molecule in its ground and bright excited states, whereas TDDFT calculations are performed through a selected combination of hybrid functionals and basis sets to obtain optical spectra closely matching the experimental findings. Solvent effects, crucial to obtaining good accuracy, are taken into account through explicit molecules and polarizable continuum descriptions. Although, in the case of toluene, specific solvation is not fundamental, the detailed conformational sampling in solution has confirmed the importance of a dynamic description of the molecular geometry for a reliable description of the photophysical properties of the dye. The agreement between theoretical and experimental data is established, and a robust protocol for the prediction of the optical behavior of flexible fluorophores in solution is set.



## 1. INTRODUCTION

Organic dyes<sup>1</sup> have recently attracted growing attention, thanks to their wide range of applications that covers different fields in both materials<sup>2–11</sup> and life sciences.<sup>12–15</sup> In particular, the high selectivity and specificity of some fluorescent molecules in detecting particular molecular targets and/or in modulating the responses to different external stimuli are often exploited to investigate the structural and dynamic properties of a wide variety of complex systems like, e.g., polymeric materials, DNA structures, protein conformations, or lipid aggregates.<sup>13</sup> In this context, the strong influence of the environment on the fluorescence properties turns out to be a fundamental key in several applications aimed to the design of new technological devices and biomimetic systems. For example, the encapsulation of a dye in a nanoparticle can enhance its fluorescence by altering the dye's flexibility and protecting it from external quenching agents,<sup>5</sup> whereas in mechanochromic materials the optical properties of the dyes are transferred to the whole system, through dispersion of the doping agent in matrices or by grafting it to polymer chains. Indeed, the interaction between the two species (i.e., the polymer and the dye) can be tuned by mechanical stress, in order to properly control both the absorption and emission responses.<sup>8,9,11</sup>

Spectroscopic techniques are becoming the methods of choice for deeper investigations of the photophysical properties

of composite materials.<sup>16–18</sup> Unfortunately, often experimental measures alone are not sufficient to unravel the subtle interplay of several effects in determining the overall result. In such circumstances, their synergistic combination with computational approaches can be effectively used both to validate experimental assignments and to provide interpretations of the results in terms of chemical structure, conformational readaptation, and molecular motion. Although computational methods can be nowadays applied directly to the study of very complex systems,<sup>18</sup> their profitable use also by nonspecialists requires the definition, implementation, and validation of robust and general computational protocols. As a matter of fact, quantum mechanical (QM) calculations are unavoidable for spectroscopic characterizations, and in the specific field of electronic spectroscopy (both absorption and emission), Time Dependent Density Functional Theory (TDDFT) has undoubtedly become the most widespread method.<sup>19</sup> Although some problems have yet to be fully solved for multiple excitations, charge transfer, and Rydberg states, for conventional valence excitations TDDFT based on hybrid (possibly range-separated) density functionals shows a nearly optimal balance between accuracy (related also to the continuous improvement of

Received: July 4, 2013

Published: September 11, 2013

functionals) and computational inexpensiveness.<sup>19–22</sup> In this framework, the energy difference (or vertical energy, VE) between the ground (GS) and the electronically excited state (EES), which leads to the VE absorption ( $\lambda_{\text{VE}}^{\text{abs}}$ , computed at the GS equilibrium geometry) or emission ( $\lambda_{\text{VE}}^{\text{abs}}$ , calculated at the EES equilibrium geometry) wavelengths, can be calculated rather straightforwardly.<sup>19</sup> Unfortunately, these quantities alone are not always sufficient to reproduce the experimental band shapes, and they cannot be directly compared to the measured maximal absorption ( $\lambda_{\text{max}}^{\text{abs}}$ ) or emission ( $\lambda_{\text{max}}^{\text{emi}}$ ) wavelengths.<sup>19,23</sup> In order to reproduce the overall line shapes and their complex features and to reach a more reliable comparison with experimental observations, it is mandatory to take nuclear motions (both of the chromophore and of its environment) into proper account.<sup>23–27</sup> In the case of flexible molecules in condensed phases, some sampling of large parts of the potential energy surfaces (PES) becomes mandatory,<sup>5,15,28–30</sup> and the most suitable approach is based, in our opinion, on molecular dynamics (MD) simulations followed by proper averaging (and smoothing) of TDDFT results for a sufficient number of representative snapshots. Implicit solvation methods, such as the Polarizable Continuum Model (PCM<sup>31</sup>), offer the undeniable advantage of correctly describing the average polarization of the environment and its effect on the chromophore without any explicit sampling of solvent coordinates, but they are, of course, unable to capture specific solvent effects, especially in the cybotactic region.<sup>26,30</sup> This has led to the proposal of an integrated discrete/continuum model able to describe both short-range and bulk solvent effects in a fully dynamical framework. The so-called GLOB model enforces nonperiodic boundary conditions (NPBC) around a rather large cluster of explicit solvent molecules by means of both PCM reaction field and specific short-range potentials minimizing boundary effects.<sup>32,33</sup> Several applications in recent years confirm the reliability and robustness of the GLOB and other related approaches.<sup>34–42</sup> Although the classical MD step can be performed also employing conventional periodic conditions in order to use standard codes (here GROMACS), NPBCs are more suitable for QM computations based on localized basis sets. Then the extraction of representative frames can be carried out following different schemes. Within the simple “mechanical embedding” (ME) scheme, for instance, only the dye coordinates are extracted from each snapshot, and the environmental effects are retained only in the solute geometrical variations induced by the presence of the surrounding *medium*. Conversely, in the “electrostatic embedding” (EE) scheme, the direct electrostatic interaction between the dye and the surrounding environment is accounted for also in the TDDFT calculations. Indeed, the EE snapshots are obtained by extracting both solute and a relevant region of the surrounding *medium* from MD trajectories, and the TDDFT calculation is thereafter performed by adopting a full QM description for the dye, a simple (possibly polarizable<sup>43–45</sup>) point charge description for the retained surrounding environment, and a PCM description of the rest of the solvent. The spectra obtained with “dynamic” approaches are then suitable for a direct comparison with the experimental line shapes: they retain information not only on the peak wavelengths but also on the broadening and shape of the absorption and emission profiles. Moreover, the simulation of resolved spectra of dyes that are optically active within the visible region makes it possible to predict their actual color, as perceived by the human eye.<sup>30,46</sup>

In order to reproduce reliably the spectroscopic properties of composite systems, MD simulations should be based on very accurate and specific force fields (FFs). Although a lot of work has been done to describe GS structures and reliable FFs are available in the literature, much less effort has been devoted to the development of “ad hoc” FFs for the EES conformations.<sup>35,47–50</sup> Recently, the Joyce<sup>51</sup> parametrization protocol, devised to obtain accurate and specific FFs from QM computed data, has been extended to the automated treatment of both GS and EES.<sup>50</sup>

In the present work, the above-mentioned “dynamic” approach is applied to compute the electronic spectra of a flexible dye, namely the 4-naphthoxyloxy-1-methoxy-2,2,6,6-tetramethylpiperidine (NfO-TEMPO-Me) molecule (see Figure 2), in toluene solution, where solvent molecules are modeled explicitly. This compound is interesting because of its potential application in the design of “smart” polymers with mechanochromic attributes as proven by the experimental characterization obtained through spectroscopic techniques and reported in a recent paper.<sup>52–54</sup> More specifically, the 2,2,6,6-tetramethylpiperidine-1-oxyl (TEMPO) unit was used, in combination with functionalizing groups such as hydroxyl, benzyl, and naphthyl (HO-, BzO-, and NfO-TEMPO), for grafting the fluorescent probe to polyethylene derivatives via postreactor modification.<sup>52,53</sup> The NfO-TEMPO derivative, substituted with a methyl group at the grafting site, has been studied from both experimental and theoretical points of view in toluene solution.<sup>53,54</sup> The theoretical analysis<sup>54</sup> depicted a complex conformational landscape, containing six stable conformers, characterized by different values of the three flexible dihedral angles describing the relative orientation of the naphthyl moiety and the TEMPO ring system (see Figure 2). Although this flexibility would suggest that several conformers contribute to the overall spectral shape, previous results<sup>54</sup> indicate that a conventional approach, employing vertical excitation calculations at the TDDFT/PCM level, performs well in reproducing experimental results at least concerning the positions of peak maxima in both absorption and emission spectra. Here, the previous computational study is extended toward a statistical approach, with the two-fold aim of achieving a more realistic sampling of the NfO-TEMPO-Me dye and solvent conformations and possibly gaining a deeper insight into the structural and dynamic features that tune the spectroscopic characteristics of the system. From a more general point of view, the present study represents a further validation of a multilevel computational approach. The good result obtained on this system encourages one to prove the reliability of the established method on more complex materials such as functionalized polymers<sup>52,53</sup> and other types of composite systems.

## 2. COMPUTATIONAL DETAILS

**2.1. General Approach.** The multilevel approach adopted in the present work is sketched in Figure 1 and can be summarized as follows.

(i) QM calculations are performed on the target molecule, to sample the conformational space of both GS and EES, identify their minima, and compute both the energy and its first and second derivatives at stationary points. Further geometry optimizations are performed at selected values of soft variables in order to better define specific FF terms (*vide infra*).

(ii) QM data are used by Joyce in two separate FF parametrizations of GS and EES, respectively.

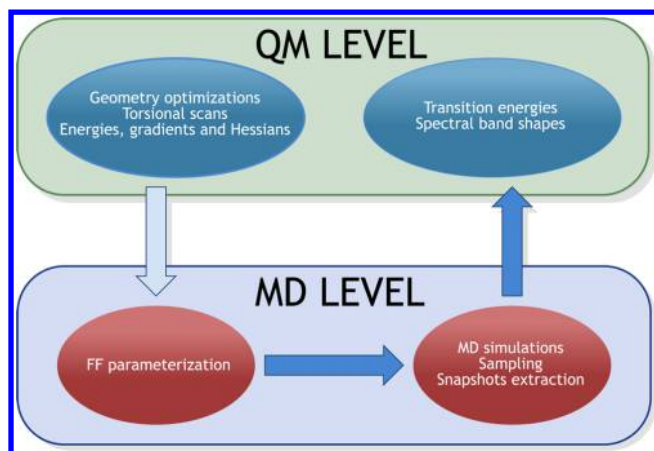


Figure 1. Scheme of the multilevel approach.

(iii) GS and EES parametrized FFs are employed in MD simulations of the target dye surrounded by explicit solvent molecules (toluene) employing periodic boundary conditions. The MD trajectories are sampled during the dynamics, and representative solute geometries are extracted, with (EE) and without (ME) explicit solvent molecules.

(iv) All the resulting mechanically and electrostatically embedded structures are employed in TDDFT QM calculations to compute the transition energies to the first EESs adding to EE structures only a PCM description of bulk solvent effects.

(v) The transition energies obtained from the GS and EES snapshots are finally combined to yield the absorption and emission spectra, respectively.

**2.2. QM Calculations.** The conformational search of NfO-TEMPO-Me in toluene solution was performed in a previous study.<sup>54</sup> Starting from the most stable conformers identified in that investigation, DFT and TDDFT geometry optimizations in the gas phase, for the GS and EES, respectively, were carried out using the PBE0 hybrid exchange-correlation functional and the N07D basis set.<sup>55,56</sup> For these optimized structures, gradients, Hessian matrices, and harmonic vibrational frequencies were calculated at the same level of theory. Moreover, QM energy scans along the  $\delta_1$ ,  $\delta_3$ , and  $\delta_4$  flexible dihedrals (see Figure 2) were performed by varying each dihedral angle from 0° to 360°, in steps of 30°, minimizing the energy without any constraint but the scanned coordinate. All electronic transitions were computed by means of the TDDFT method on the ME and EE snapshots extracted from the MD simulations, considering the seven lowest transitions for each frame. As far as the EE snapshots are concerned, toluene molecules extracted from the MD frames were replaced by fixed atomic point charges, whereas bulk solvent effects were accounted for through the PCM approach.<sup>31</sup> The direct electrostatic effect of the solvent on the electronic property is entirely neglected in the ME scheme, by switching off both the implicit and the explicit solvation shells. The performances of different functionals, namely PBE0 and CAM-B3LYP, in combination with N07D<sup>57</sup> and cc-pvDz basis sets, were explored.

The Gaussian 09 suite of programs<sup>58</sup> has been used to carry out all QM calculations.

**2.3. FF Parametrization.** The intramolecular FF employed for the description of NfO-TEMPO-Me,  $E^{\text{intra}}$ , takes the standard form

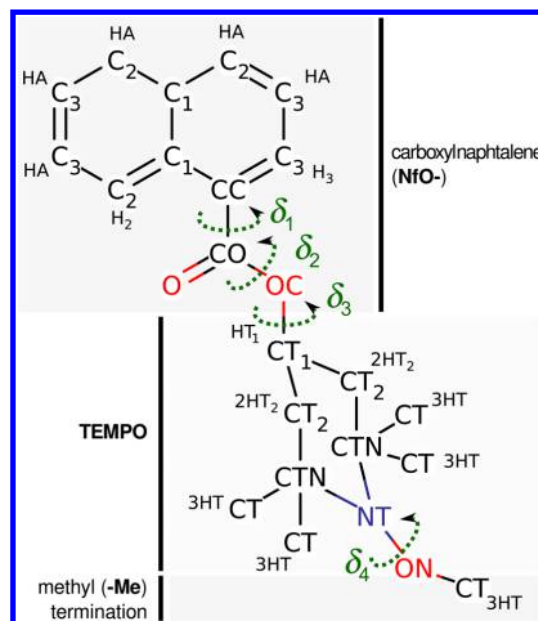


Figure 2. The NfO-TEMPO molecule. The atom types employed in the force field and the four main flexible dihedrals are shown.

$$E^{\text{intra}} = E^{\text{stretch}} + E^{\text{bend}} + E^{\text{Rtors}} + E^{\text{Ftors}} + E^{\text{nb}} \quad (1)$$

where the first three terms are represented by harmonic expressions

$$\begin{aligned} E^{\text{stretch}} &= \frac{1}{2} \sum_{\mu}^{N_s} k_{\mu}^s (r_{\mu} - r_{\mu}^0)^2 \\ E^{\text{bend}} &= \frac{1}{2} \sum_{\mu}^{N_b} k_{\mu}^b (\theta_{\mu} - \theta_{\mu}^0)^2 \\ E^{\text{Rtors}} &= \frac{1}{2} \sum_{\mu}^{N_{\text{Rt}}} k_{\mu}^t (\phi_{\mu} - \phi_{\mu}^0)^2 \end{aligned} \quad (2)$$

In eq 2,  $k_{\mu}^s$ ,  $k_{\mu}^b$ , and  $k_{\mu}^t$  and  $r_{\mu}^0$ ,  $\theta_{\mu}^0$ , and  $\phi_{\mu}^0$  are the force constants and equilibrium values for stretching, bending, and stiff torsional internal coordinates,<sup>50</sup> respectively. The potential energies governing rotations around dihedrals  $\delta_1$ – $\delta_4$  are described by sums of cosines, namely

$$E^{\text{Ftors}} = \sum_{\mu}^{N_{\text{Fdihedrals}}} \sum_{j=1}^{N_{\mu}} k_{j\mu}^d [1 + \cos(n_{\mu}^j \delta_{\mu} - \gamma_{\mu}^j)] \quad (3)$$

where  $k_{j\mu}^d$  is the force constant;  $\delta_{\mu}$ , the dihedral; and  $n_{\mu}^j$  and  $\gamma_{\mu}^j$ , the multiplicity and a phase factor for the  $j$ th cosine.  $N_{\mu}$  is the number of cosine functions employed for dihedral  $\mu$ . The last term of eq 1 is computed as

$$E^{\text{nb}} = \sum_{i=1}^{N_{\text{sites}}} \sum_{j=1}^{N_{\text{sites}}} [E_{ij}^{\text{nb intra}}] \quad (4)$$

where the interaction between the  $i$ th and  $j$ th atoms is described through a 12–6 Lennard-Jones (LJ) plus Coulomb charge–charge potential ( $E^{\text{nb intra}}$ ).

Both the solute GS and EES FFs were parametrized with the JOYCE package,<sup>50,51</sup> through a least-squares minimization of the functional  $I^{\text{intra}}$



$$I^{\text{intra}} = \sum_{g=0}^{N_{\text{geom}}} W_g [U_g - E_g^{\text{intra}}]^2 + \sum_{K \leq L}^{3N-6} \frac{2W_{KL}''}{(3N-6)(3N-5)} \left[ H_{KL} - \left( \frac{\partial^2 E^{\text{intra}}}{\partial Q_K \partial Q_L} \right) \right]_{g=0}^2 \quad (5)$$

where  $N_{\text{geom}}$  is the number of the sampled conformations,  $Q_K$  is the  $K$ th normal coordinate, and  $U_g$  is the QM computed energy in the  $g^{\text{th}}$  geometry, with respect to the absolute minimum ( $g = 0$ ). The QM Hessian matrix  $H_{KL}$  and the FF Hessian are evaluated at  $g = 0$ . All the geometry weights  $W_g$  are set to the same unitary value; the diagonal and off diagonal weights of the Hessian matrix elements  $W_{KL}''$  are set to 5000 and 2500, respectively. More details on the minimization procedure can be found in previous works.<sup>50,51</sup>

As far as the interaction of the NfO-TEMPO molecule with the solvent is concerned, the standard 12–6 LJ plus charge–charge potential was adopted. For the solute, LJ intermolecular parameters were taken from the OPLS FF,<sup>59,60</sup> and the atomic point charges were obtained from the equilibrium GS and EES QM geometries through the CMS procedure.<sup>61</sup> Conversely, OPLS literature parameters<sup>59</sup> were employed for the solvent in all simulations, i.e., with the solute in its ground or excited state.

**2.4. MM Optimizations and MD Simulations.** Full or partial energy optimizations at the MM level were performed using the conjugate gradient algorithm available within the Gromacs 4.5.4 package.<sup>62</sup> Structures were minimized with a convergence threshold on the root-mean-square forces of 1 kJ·mol<sup>−1</sup>·nm<sup>−1</sup>. Harmonic dihedral restraints of 1000 kJ·mol<sup>−1</sup> were imposed on the scanned internal dihedrals when needed.

All the MD simulations were carried out with GRO-MACS4.5.4.<sup>62</sup> The GS and EES FFs of the dye were employed for both simulations *in vacuo* and in solution. The system simulated in solution consisted of one NfO-TEMPO-Me molecule inserted in a cubic box and surrounded by 991 toluene molecules. Periodic boundary conditions were applied in all directions, and the simulation time step was set to 0.5 fs. Long-range electrostatic interactions were treated with the particle mesh Ewald (PME) method, whereas a 14 Å cutoff was applied to the van der Waals interactions. The production run was preceded by an equilibration phase during which the starting configuration was first energy minimized, to remove unfavorable steric interactions. The resulting configuration was subjected to a further equilibration protocol coupling the system to a thermal bath at temperature  $T = 300$  K (with a coupling constant of 0.1 ps) and a pressure bath with pressure  $P = 1$  atm (with a coupling constant of 1.0 ps) for a total period of 1 ns. Starting from the final structure, 3 ns of production dynamics were carried out in the NPT ensemble. During both the equilibration and production phases, Berendsen's weak coupling schemes<sup>63</sup> were employed. Configurations were stored every 0.5 ps for further analysis. Simulations in the gas phase were performed in the NVT ensemble at 300 K, and the total sampling time was 1.2 ns. Selected snapshots were extracted from the MD trajectories and used for the simulations of the spectra. The samples consisted of 80 and 200 configurations for the simulation in the gas phase and in solution, respectively. In the latter case, two sets of snapshots were extracted, for the ME and EE schemes, containing respectively only the solute or the solute plus all toluene molecules within a radius  $R_{\text{cut}}$  from its center of mass.

**2.5. Statistical Calculation of the UV–Vis Spectra.** The transition energies computed on each set of snapshots were convoluted with Gaussian functions in the energy domain with a half width at half-maximum (HWHM  $\Delta_\nu$ ) of 0.05 eV. Thus, the spectrum computed for the  $c$ th frame is

$$\varepsilon_c(\nu) \propto \sum_{i \in \text{states}_c} \frac{f_{c,i}}{\Delta_\nu} \exp \left[ - \left( \frac{\nu - \nu_{c,i}^0}{\sigma_\nu} \right)^2 \right] \quad (6)$$

where  $h\nu_{c,i}^0$  and  $f_{c,i}$  are the energy and the oscillator strength of the  $i$ th excited state, respectively, whereas  $\sigma_\nu = [2(2 \ln(2))^{1/2}]^{-1} \Delta_\nu$ . For a *vis-à-vis* comparison with the experimental data, the energy spectrum is then plotted in the wavelength domain ( $\varepsilon_c(\lambda)$ ). The signals originating from each snapshot are then averaged according to the equation

$$\bar{\varepsilon}(\lambda) = \sum_{c \in \text{snap}} \frac{\varepsilon_c(\lambda)}{N_{\text{snaps}}} \quad (7)$$

to achieve the final “statistical” UV–vis spectrum for a given functional-basis choice.

### 3. RESULTS

**3.1. NfO-TEMPO FF Parametrization.** As indicated in section 2, NfO-TEMPO intermolecular parameters were transferred from OPLS<sup>59,60</sup> FF (LJ) or obtained from QM data (CMS point charges). The atom types chosen to model the NfO-TEMPO molecule, for both GS and EES, are reported in Figure 2. All intermolecular parameters can be found in the Supporting Information.

The intramolecular FF parametrization was performed by minimizing the functional (eq 5), achieving standard deviations of 0.172 and 0.165 kJ/mol for GS and EES, respectively. Inspection of Table 1 (where a selected set of the optimal parameters is reported) shows that the parametrized FF is able to capture even subtle differences between similar internal coordinates that could not be distinguished by general purpose FFs. In the GS parametrization, for instance, a non-negligible difference is found between the C1–C2 and the C2–C3 aromatic bonds in the naphthalene moiety, which are described by slightly different equilibrium distances (1.42 and 1.38 Å) and remarkably different force constants (2954 and 3897 kJ/mol Å<sup>−2</sup>, respectively). Structure rearrangements taking place upon electronic transition are also accounted for, as indicated by the changes shown by FF parameters between the GS and EES FF. For instance, the CC–CO equilibrium bond distance decreases from 1.49 Å to 1.45 Å and the relative force constant increases by ~500 kJ/mol Å<sup>−2</sup>, paralleling the partial  $\pi$  character that the bond assumes in the EES. It is worth noticing that in the EES, as a result of the increased delocalization of the naphthalene  $\pi$  cloud toward the carboxyl region, the naphthalene structure reduces its conjugate character and consequently its rigidity, as can be seen from the decrease by ~50 kJ/mol of the harmonic improper dihedral terms describing the out-of-plane deviations in the region.

Broadly speaking, the force constants relative to the internal coordinates of the carboxynaphthalene group show rather substantial differences between GS and EES: changes as large as 22%, 47%, and 31% are found for the stretching, bending, and torsion harmonic terms, respectively. Instead, negligible modifications were found in the parameters relative to the TEMPO-Me region, with deviations on the stretching and

**Table 1.** Selected FFs Parameters for NfO-TEMPO-Me as Optimized by Joyce

moiety	bonds	GS		EES	
		$r^0$	$k^s$	$r^0$	$k^s$
NfO	C2–C3	1.38	3897	1.42	3033
	C3–C3	1.41	3341	1.38	3801
	C1–CC	1.44	2554	1.44	2498
	C3–CC	1.38	3507	1.44	2763
	CC–CO	1.49	2034	1.45	2489
	CO–O	1.21	6703	1.23	5682
	CO–OC	1.35	2936	1.36	2848
	OC–CT1	1.44	2390	1.43	2441
TEMPO-Me	CT1–CT2	1.52	2276	1.52	2226
	CT2–CTN	1.54	1936	1.54	1924
	CTN–NT	1.49	2053	1.49	2036
	NT–ON	1.42	2444	1.42	2416
	ON–CT	1.41	2491	1.41	2503
moiety	angles	$\theta^0$	$k^b$	$\theta^0$	$k^b$
NfO	C2–C1–C1	118	581	118	383
	C2–C1–CC	124	805	123	709
	C2–C3–C3	121	648	119	581
	C1–CC–CO	122	420	122	234
	O–CO–OC	122	968	121	1013
TEMPO	CO–OC–CT1	117	727	117	661
moiety	harmonic dihedrals	$\phi^0$	$k^t$	$\phi^0$	$k^t$
NfO	C*–C*–C*–C* ( <i>cis</i> )	0	53.6	0	47.6
	C*–C1–C1–C2 ( <i>trans</i> )	180	53.6	180	47.6
	H*–C*–C*–C* (o.o.p.)	0	554.2	0	490.4
	O–CO–OC–CT1 ( $\delta_2$ )	0	30.3	0	30.3
	CC–O–OC–CO (o.o.p.)	0	928.6	0	670.5
moiety	periodic dihedrals	$n^i$	$k_j^d$	$n^i$	$k_j^d$
TEMPO	OC–CT1–CT2–CTN	3	8.95	3	7.77

The atom types are reported in Figure 2. The equilibrium coordinates  $r^0$ ,  $\theta^0$ , and  $\phi^0$  (reported in Å and deg, respectively) and the force constants  $k^b$ ,  $k^t$ , and  $k_j^d$  (in kJ/mol Å<sup>−2</sup>, kJ/mol rad<sup>−2</sup>, and kJ/mol) have been defined in eqs 1–3. The complete parameter set can be found in the Supporting Information.

bending harmonic terms lower than 2% and 8%, respectively. A tentative explanation lies in the fact that NfO-TEMPO-Me HOMO and LUMO orbitals are essentially localized on the carboxynaphthalene portion of the molecule<sup>54</sup> that can thus be considered the most relevant part in the description of the optical behavior of this compound.

The capability of the new FF to reproduce correctly the vibrational behavior of the molecule is quantified by comparing the harmonic frequencies computed at the QM and MM levels (see Figure 3). A good agreement is achieved, resulting in a root-mean-square deviation of 38 and 37 cm<sup>−1</sup>, for GS and EES, respectively. It may be worth noting that the achieved accuracy is in line with the results obtained in previous parametrizations,<sup>50</sup> hence a rather reliable representation of the NfO-TEMPO vibrational behavior is expected during MD simulations.

As far as the flexible dihedral angles,  $\delta_1$  and  $\delta_3$ , are concerned, they are expected to affect the conformation of the NfO moiety, and therefore, for each dihedral, the reference QM torsional energy scan was performed separately for GS and EES. Conversely, for computational convenience, the QM  $\delta_4$  scan was performed only for GS, and the resulting FF parameters were simply transferred from the GS to the EES FF. For all dihedrals, both FFs accurately match their QM reference

energy profile. In the top panel of Figure 4, the QM energies calculated for the optimized geometries at a given torsional angle are compared to their MM counterparts, showing a very good agreement for both GS and EES. As could be expected considering the localization of the HOMO and LUMO orbitals,<sup>54</sup> major differences between GS and EES profiles were found, at both QM and MM levels, only for  $\delta_1$ , whereas the  $\delta_3$  torsional curve does not undergo noticeable changes upon electronic transition. The different steepness around the  $\delta_1$  minimum is also in agreement with the partial  $\pi$  character of the CC–CO bond revealed by the force constants analysis.

On the grounds of earlier studies,<sup>34,35</sup> it is expected that the dihedral description strongly affects the optical properties of the molecule. The absorption and emission wavelengths  $\lambda_{\text{VE}}^{\text{abs/em}}i$  have been calculated, at the VE TD-DFT level, for all the QM and MM geometries, obtained in the torsional energy scans. The results are shown in the bottom panel of Figure 4. As a matter of fact, both absorption and emission wavelengths for QM and MM optimized geometries show a strong dependence on the  $\delta_1$  angle, which is responsible for the relative orientation of the naphthyl and carboxyl moieties within the NfO portion of the molecule. The values computed for the MM geometries are in good agreement with those identified by the QM calculations, with slightly larger differences (+6.0 nm for absorption and +11.1 nm for emission) in the case of  $\delta_1 = 180^\circ$ . Nonetheless, the latter conformation is expected to be scarcely populated at room temperature, considering its relative stability ( $\approx 12$  kJ/mol) and high interconversion barrier ( $\approx 60$  kJ/mol) with respect to the absolute energy minimum (at  $\delta_1 = 0^\circ$ ). As long as  $\delta_3$  is concerned, its effect on  $\lambda_{\text{VE}}^{\text{abs/em}}i$  is less pronounced, with some minor variations found in emission for  $\delta_3 \sim 30^\circ$ . This scarce sensitivity is not surprising, considering that the HOMO and LUMO orbitals are localized in molecular regions not involved in the  $\delta_3$  torsion. As for  $\delta_1$ , the FF mimics with rather good accuracy this behavior, with slightly larger deviations for absorption, found in high energy conformations ( $\delta_3 < -60^\circ$ ).

**3.2. Simulations.** The GS and EES parametrized FFs were employed in two sets of MD simulations, performed on the isolated dye at 300 K and on the solvated NfO-TEMPO at 1 atm and 300 K. All four systems (i.e., GS and EES *in vacuo* and solvated GS and EES) were equilibrated for 1 ns and subsequently simulated for 1.2 and 3 ns (for the *in vacuo* and solvated phase, respectively), saving trajectories every 0.5 ps.

The dye internal structure, along the four different simulations has been first evaluated by looking at the distributions of the two main flexible dihedrals, reported in Figure 5. As regards the GS simulation in the gas phase (black dotted line),  $\delta_1$  remains constrained into the main potential well, and its distribution is symmetrically broadened around  $0^\circ$ , the QM reference value being within this well, at about  $-12^\circ$ . The solvated system shows similar distributions within the  $\delta_1 \approx 0^\circ$  region, but the interaction with the solvent allows for exploring also the local minimum at about  $180^\circ$ . Conversely, due to the increased steepness around the  $\delta_1$  minimum region found in the torsional profile, the EES population distribution is much narrower for both isolated and solvated systems, and the  $180^\circ$  region is never explored. As a consequence, any possibility for  $\delta_1$  to be trapped in the above-mentioned region (either by vertical excitation from the GS or internal conversion from higher EES) is neglected at this level. The  $\delta_3$  distribution shows, instead, a double peak for both GS and EES simulations, with the first one corresponding to the QM value of about  $85^\circ$

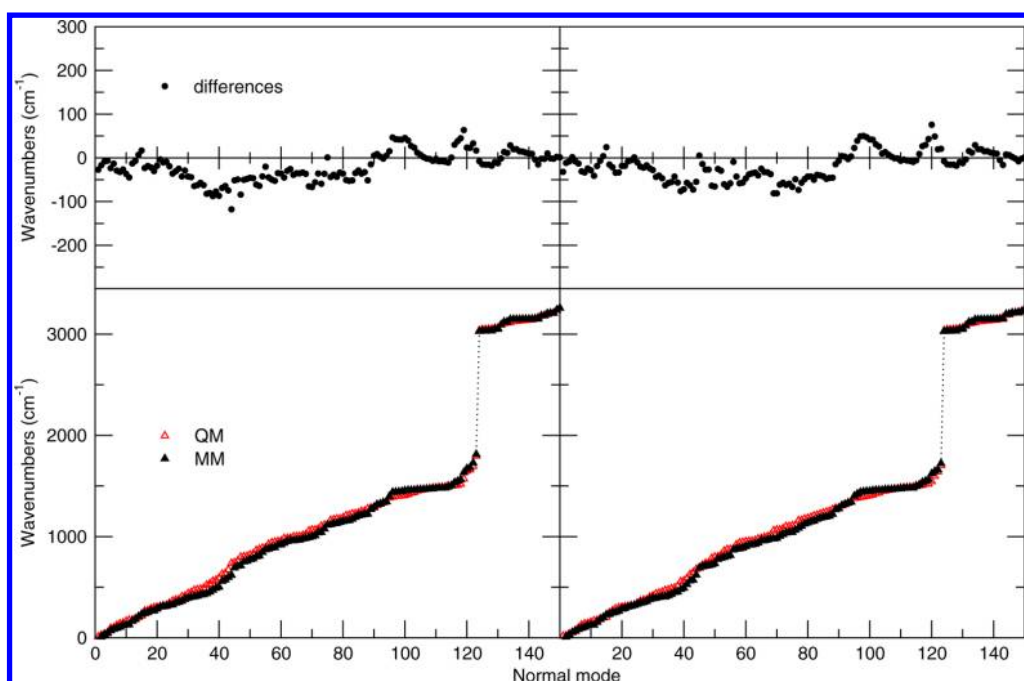


**Figure 3.** NfO-TEMPO vibrational frequencies in GS and EES. Bottom: comparison between QM and MM computed frequencies. Top: differences between the two descriptions.

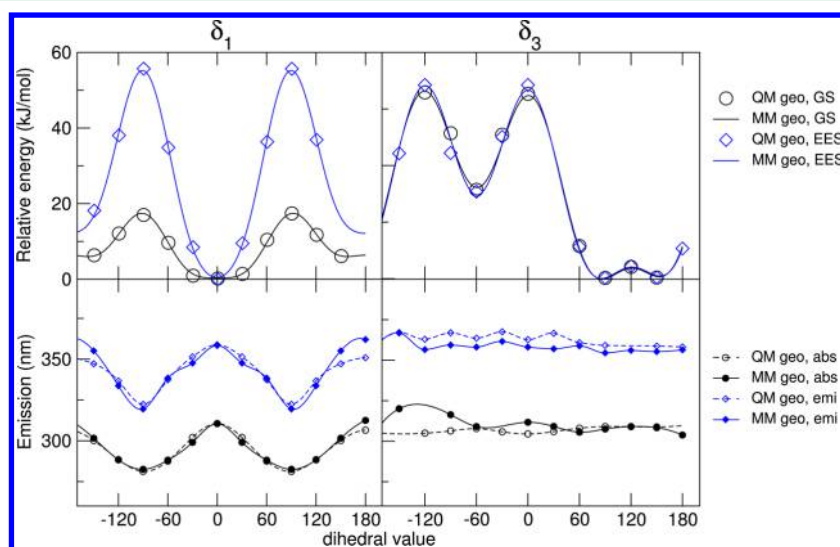


**Figure 4.** FF description of the dihedral angles. Top: energy profiles along the  $\delta_1$  and  $\delta_3$  internal dihedrals for GS and EES, at the QM and FF level. Bottom: single point excitation wavelengths at partially optimized QM and MM geometries.

and the second one located at  $\delta_3 \simeq 150^\circ$ , i.e., close to the second local minimum found in the torsional energy scan reported in Figure 4.

Furthermore, as the solvated systems are concerned, the local solvent structure around the dye has been monitored by computing the pair correlation function between the NfO-TEMPO and toluene centers of mass, for both GS and EES. Inspection of Figure 6 shows that some differences arise in the first solvation shell for GS and EES, the number of first neighbors being larger in the latter case. On the other hand, the differences become negligible for the second solvation shell, and at distances larger than 13 Å, both pair correlation functions converge to a homogeneous density. Clearly, a continuum model is unable to account for these local features, and for this reason a portion of the surrounding solvent was

included in the snapshots extracted for the EE calculations. In particular, all solvent molecules within a radius  $R_{\text{cut}}$  of 15 Å were included explicitly. Indeed, beyond this distance, the pair correlation function has reached its asymptotic value, and the PCM can be confidently applied, as shown pictorially in the right panel of Figure 6. The included solvent molecules amount on average to 30, with a standard deviation of 2, for both GS and EES simulations.

**3.3. Absorption Spectra.** Snapshots spaced by constant time intervals are then extracted from the MD simulations and used to calculate the UV/vis spectra with an integrated TD-DFT/charges/PCM computational setup. In Figure 7, top panel, a typical unconvoluted absorption spectrum from a random frame is shown in black bars. A Gaussian broadening was applied according to eq 6 with two different values for  $\Delta_\nu$ :



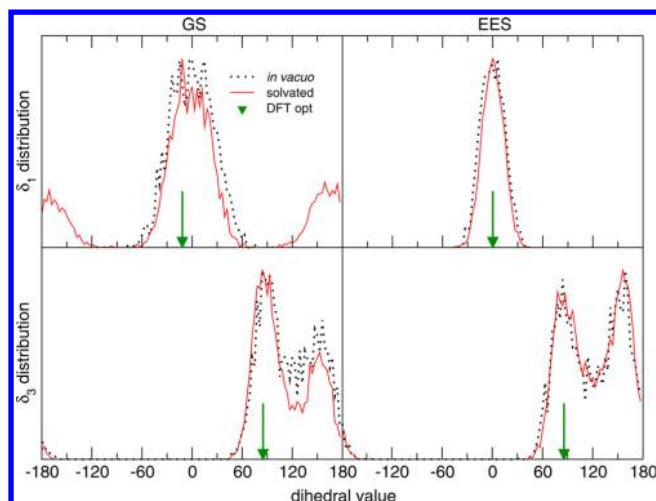


**Figure 5.** Distributions of the  $\delta_1$  (top) and  $\delta_3$  (bottom) dihedrals during the simulations, compared to the QM optimized geometry. The curves are normalized to their maximum value. For NfO-TEMPO-Me, the ground state (left) and the electronically excited state (right) are considered.

0.25 eV is the value used in the previous time-independent study of NfO-TEMPO-Me,<sup>54</sup> whereas 0.05 eV is the value chosen for the present work. In the bottom panel, the absorption spectrum is obtained by averaging, over an increasing number of snapshots, the signals broadened with  $\Delta_\nu = 0.05$  eV for each frame. It should be noted that the overall spectrum results now from the sum of hundreds of Gaussian functions, centered at different positions, that converge to a smooth, averaged line when the sampling is reliable. The inclusion of one frame every 15 ps of MD is chosen for all the computations in the following, in order to achieve a smooth statistical description without artifacts arising from the sampling itself. The dynamic approach proposed in the present study red-shifts the absorption wavelength,  $\lambda_{\text{max}}^{\text{abs}}$ , by about 2 nm, with respect to the static approach employed in a previous work.<sup>54</sup> Unfortunately, the static value (315 nm) did already overestimate the experimental  $\lambda_{\text{max}}^{\text{abs}}$  by 16 nm, so that dynamical effects seem to worsen agreement with experimental results. Since the choice of the functional/basis set could play a role in determining this trend, other functional/basis set pairs have been explored, eventually obtaining remarkably accurate results by combining the CAM-B3LYP functional with the cc-pvDz

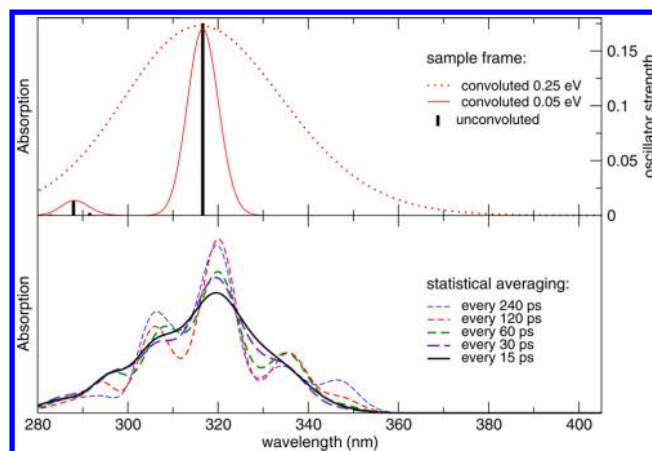


**Figure 7.** Statistical averaging of UV/vis spectra of absorption. Top: the stick spectrum calculated from a sample snapshot of the GS dynamics in toluene at the PBE0/N07D level of theory, convoluted using different values for  $\Delta_\nu$ . Bottom: average signal from the 5 ns MD exploiting an increasing number of snapshots and  $\Delta_\nu = 0.05$  eV.

basis set (see Figure 8). In this case, the static approach (black placemark in the graph) underestimates the experimental peak

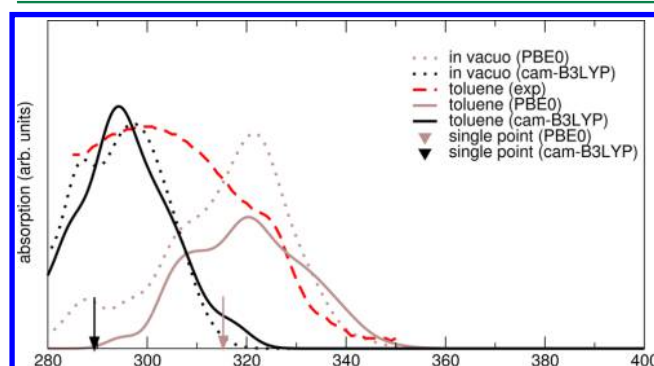


**Figure 8.** Absorption spectra *in vacuo* (dotted) and in toluene solution (solid line) calculated with different DFT XC functionals (PBE0, brown; cam-B3LYP, black) in the statistical approach, compared to the static approach (placemarks) and to the experimental spectrum. The same normalization was used for all the computed spectra.

wavelength by 10 nm, but this error is corrected by the MD treatment with a 3 nm red-shift. The *thermal* broadening of the

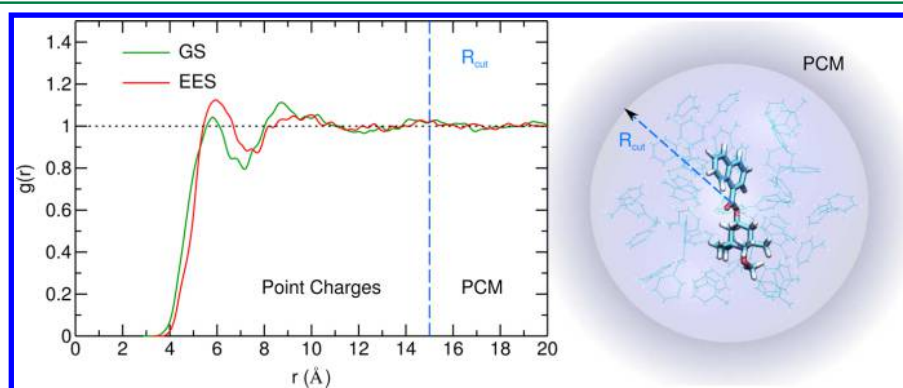


**Figure 6.** Left panel: solute-solvent pair correlation functions relative to the GS and EES simulations. Right panel: layered hybrid description of the dye in solution. The dye is described at the QM level; a 15 Å large sphere of explicit toluene atomic charges is placed around it and is embedded in a spherical PCM cavity.

absorption line, obtained by including different snapshots, allows a more direct comparison of the spectra, resulting in good agreement between the computed and the experimental<sup>54</sup>  $\lambda_{\text{max}}^{\text{abs}}$  (292 and 299 nm, respectively). Concerning solvent effects, it should be noted that solvatochromic shifts are quite negligible, leading to very similar spectra in the gas phase and in solution.

**3.4. Emission Spectra.** Emission spectra were computed at the CAM-B3LYP/cc-pvDz level with the same approach adopted for absorption, and the resulting spectral lines are reported in Figure 9. Inspection of the figure shows that the

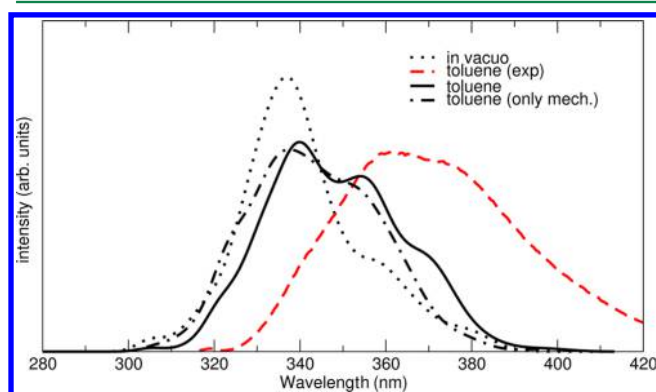


**Figure 9.** Emission spectra calculated in the statistical approach with the cam-B3LYP functional compared to the experimental spectrum. The spectra are calculated *in vacuo* (dotted) and toluene solution (solid line), considering also the “mechanical embedding” alone (dash-dotted line).

emission profile of NfO-TEMPO-Me in toluene solution reproduces fairly well the experimental data, especially the line-shape and its decay, although the peak is blue-shifted by about 15 nm. At variance with absorption, the effect of the solvent on the spectral shape is quite significant. In this case, the spectrum in the gas phase is less broadened and centered at a shorter wavelength (by about 17 nm) so that a non-negligible solvatochromic shift is observed. It is worth noticing that the increased sensitivity to the solvent, found for EES with respect to GS, is consistent with the augmented flexibility of the naphthalene skeleton (i.e., where HOMO and LUMO orbitals are essentially localized) evidenced by the FF and with the larger number of solvent molecules found in the first solvation shell by pair correlation function analysis. A deeper insight into this solvent effect can nonetheless be gained by comparing the spectra obtained with ME and EE methods. As can be seen in Figure 9, the main contribution to the broadening is accounted for already at the ME level, whereas the inclusion of the direct

electrostatic interaction in the TDDFT calculations, achieved with EE, only tunes the signal, evidencing two shoulders at ~355 and 370 nm.

Results obtained previously with a vertical excitation approach<sup>54</sup> and with the present time dependent protocol are summarized in Table 2, whereas the final computed absorption and emission spectra are compared with their experimental counterparts in Figure 10. The dynamic approach has the clear

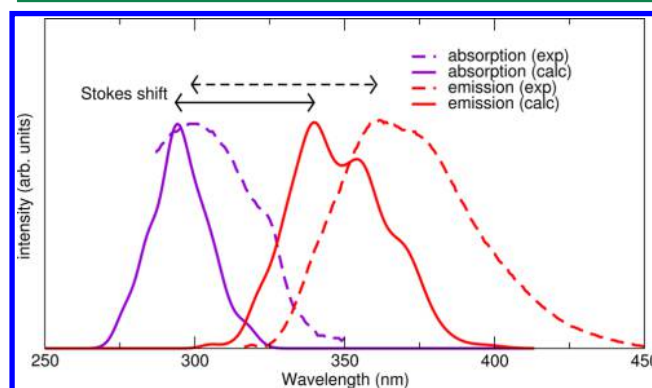


**Figure 10.** Time dependent computed (solid lines) and experimental (dotted lines) absorption and emission spectra. Stokes shift are indicated with black arrows.

advantage of providing a detailed band shape that can be directly compared with the experimental signals; moreover, it can reproduce true maximal absorption and emission wavelength  $\lambda_{\text{max}}^{\text{abs/em}}^{\text{abs/em}}$ , instead of vertical energies  $\lambda_{\text{VE}}^{\text{abs/em}}$ , which are closely related to the experimental values. Indeed, in the present case, a slightly better agreement with the experiments is also achieved. More important, the Stokes shift, which is defined as the difference between  $\lambda_{\text{max}}^{\text{emi}}$  and  $\lambda_{\text{max}}^{\text{abs}}$ , can now be computed more rigorously, yielding a good agreement (8 nm) with the experimental one.

#### 4. CONCLUSIONS

The time dependent protocol used in this work for the computation of absorption and emission spectra of the NfO-TEMPO dye in toluene solution was able to reproduce peak wavelengths, spectral line shapes, and Stokes shifts in good agreement with the experimental data. With respect to the static approach, which was previously<sup>54</sup> adopted by our group to study the NfO-TEMPO system, the description of the spectroscopic behavior of the solvated dye is significantly improved, and a more reliable comparison with the measured spectra is now possible, due to the availability of the band shapes and the consequent correct definition of  $\lambda_{\text{max}}^{\text{abs/em}}$ .

**Table 2.** Comparison of the Absorption Peak Wavelengths and the Stokes Shifts for the NfO-TEMPO-Me UV/vis Spectrum from Different Methods

method	absorption wavelength		Stokes shift	
	gas phase	toluene	gas phase	toluene
experimental <sup>a</sup>		299 nm		62 nm
single point	PBE0/N07D <sup>a</sup>	315 nm		
	CamB3LYP/cc-pvDz <sup>b</sup>	289 nm		
statistical <sup>b</sup>	PBE0/N07D	316 nm	38 nm	50 nm
	CamB3LYP/cc-pvDz	292 nm	37 nm	54 nm

<sup>a</sup>Ref 54. <sup>b</sup>This work. <sup>a</sup>TD-DFT/PCM calculations at the equilibrium geometry are referred to as single point, while the statistical approach is the one based on MD simulations.



Besides the results achieved, the choice of adopting this time dependent protocol can be *a posteriori* validated in consideration of two important features. First, an accurate representation of the molecular flexibility is found to be important. This is because there is a strong dependence of the spectral response on the molecular conformation. As a consequence, the use of a specific and reliable FF is essential when classical MD techniques are employed for the statistical sampling. Furthermore, although strong specific solute–solvent interactions are not expected in the present case, an explicit account for the solvent molecules remains essential for a correct description of EES, where both ME and EE altered remarkably the *in vacuo* computed spectral line shape

As already observed in previous works, the present protocol is well suited also for the description of more complex systems,<sup>34,35,38,39</sup> where the surrounding medium consists of advanced materials such as nanoparticles, polymers, lipid bilayers, and other types of molecular environments. Indeed, the extension of the present computational procedure to the study of the NfO-TEMPO dye in a polymeric matrix is currently in progress.

Finally, it may be important to note that, in the *in silico* design of such complex materials, the choice of a reliable combination of DFT functional and basis set is of fundamental importance. The present work suggests that the selection of the most suitable combination in the TDDFT calculations of the spectral properties should be driven by the comparison of the experimental spectra with broadened theoretical lines, rather than by single point vertical excitations. According to the more or less flexible structure of the target dye and/or to the strength of the interactions with the surrounding medium, this can be done in a time independent fashion, by accounting for the vibronic structure,<sup>27</sup> or through a time-dependent statistical approach, as done in the present work.

## ■ ASSOCIATED CONTENT

### ■ Supporting Information

The complete parameter files in GROMACS4.5.4 format, the velocity autocorrelation function of the dye throughout the MD simulation, and the dependence of the TDDFT calculation on the explicit solvent shell radius  $R_{\text{cut}}$  are provided. This information is available free of charge via the Internet at <http://pubs.acs.org/>

## ■ AUTHOR INFORMATION

### Corresponding Author

\*E-mail: nicola.demitri@sns.it.

### Notes

The authors declare no competing financial interest.

## ■ ACKNOWLEDGMENTS

The research leading to these results was supported by the European Unions Seventh Framework Programme (FP7/2007-2013) under Grant Agreement No. ERC-2012-AdG-320951-DREAMS and by the Fondazione Cassa di Risparmio di Pisa under POLOPTEL project no. 167/09.

## ■ REFERENCES

- (1) Zollinger, H. *Color Chemistry: Syntheses, Properties, and Applications of Organic Dyes and Pigments*; John Wiley & Sons: New York, 2003.
- (2) Sagara, Y.; Kato, T. *Nature Chem.* **2009**, *1*, 605–610.
- (3) X.Zhang, S.; Rehm, M. S.-S. F. W. *Nature Chem.* **2009**, *1*, 623–629.
- (4) Davis, D.; Hamilton, A.; Yang, J.; Cremer, L.; Gough, D. V.; Potisek, S.; Ong, M.; Braun, P.; Martinez, T.; White, S.; Moore, J.; Sottos, N. *Nature* **2009**, *459*, 68–72.
- (5) Larson, D. R.; Ow, H.; Vishwasrao, H. D.; Heikal, A. a.; Wiesner, U.; Webb, W. W. *Chem. Mater.* **2008**, *20*, 2677–2684.
- (6) Hagfeldt, A.; Boschloo, G.; Sun, L.; Kloo, L.; Pettersson, H. *Chem. Rev.* **2010**, *110*, 6595–6663.
- (7) Kim, H.; Guo, Z.; Zhu, W.; Yoon, J.; Tian, H. *Chem. Soc. Rev.* **2011**, *40*, 79–93.
- (8) Pucci, A.; Bizzarri, R.; Ruggeri, G. *Soft Matter* **2011**, *7*, 3689–3700.
- (9) Pucci, A.; Ruggeri, G. *J. Mater. Chem.* **2011**, *21*, 8282–8291.
- (10) Chen, Y.; Spiering, A.; Karthikeyan, S.; Peters, G.; Meijer, E.; Sijbesma, R. *Nature Chem.* **2012**, *4*, 559–562.
- (11) Ciardelli, F.; Ruggeri, G.; Pucci, A. *Chem. Soc. Rev.* **2013**, *42*, 857–870.
- (12) Nalwa, H. *Handbook of Photochemistry and Photobiology*; American Scientific Publishers: Valencia, CA, 2003.
- (13) Haugland, R. P. *The Handbook. A Guide to Fluorescent Probes and Labeling Technologies*; Molecular Probes, Inc.: Eugene, OR, 2005.
- (14) Goldys, E. *Fluorescence Applications in Biotechnology and Life Sciences*; Wiley-Blackwell: New York, 2005.
- (15) Signore, G.; Nifos, R.; Albertazzi, L.; Storti, B.; Bizzarri, R. *J. Am. Chem. Soc.* **2010**, *132*, 1276–1288.
- (16) Ellis, A.; Feher, M.; Wright, T. *Electronic and Photoelectron Spectroscopy*; Cambridge University Press: Cambridge, U. K., 2005.
- (17) Laane, J. *Frontiers of Molecular Spectroscopy*; Elsevier: Amsterdam, 2009.
- (18) Barone, V., Ed. *Computational Strategies for Spectroscopy: From Small Molecules to Nano Systems*; Wiley: Chichester, U. K., 2011.
- (19) Adamo, C.; Jacquemin, D. *Chem. Soc. Rev.* **2013**, *42*, 845–856.
- (20) Yanaia, D. P.; Tewb, N. H. *Chem. Phys. Lett.* **2004**, *393*, 51–57.
- (21) Leang, S. S.; Zahariev, F.; Gordon, M. S. *J. Chem. Phys.* **2012**, *136*, 104101–104112.
- (22) Bousquet, D.; Fukuda, R.; Maitarad, P.; Jacquemin, D.; Ciofini, I.; Adamo, C.; Ehara, M. *J. Chem. Theory Comput.* **2013**, *9*, 2368–2379.
- (23) Avila Ferrer, F. J.; Santoro, F. *Phys. Chem. Chem. Phys.* **2012**, *14*, 13549–13563.
- (24) Barone, V.; Bloino, J.; Biczysko, M.; Santoro, F. *J. Chem. Theory Comput.* **2009**, *5*, 540–554.
- (25) Bloino, J.; Biczysko, M.; Santoro, F.; Barone, V. *J. Chem. Theory Comput.* **2010**, *6*, 1256–1274.
- (26) Klauwinzer, B.; Kröner, D.; Saalfrank, P. *J. Phys. Chem. B* **2011**, *114*, 10826–10834.
- (27) Prampolini, G.; Bellina, F.; Biczysko, M.; Cappelli, C.; Carta, L.; Lessi, M.; Pucci, A.; Ruggeri, G.; Barone, V. *Chem.—Eur. J.* **2013**, *19*, 1996–2004.
- (28) Pereira Gomes, A.; Jacob, C. *Annu. Rep. Prog. Chem.* **2012**, *108*, 222–277.
- (29) Ali, M.; Dutta, P.; Pandey, S. *J. Phys. Chem. B* **2010**, *114*, 15042–15051.
- (30) Malcioglu, O. B.; Calzolari, A.; Gebauer, R.; Varsano, D.; Baroni, S. *J. Am. Chem. Soc.* **2011**, *133*, 15425–15433.
- (31) Tomasi, J.; Mennucci, B.; Cammi, R. *Chem. Rev.* **2005**, *105*, 2999–3093.
- (32) Brancato, G.; Rega, N. In *Computational Strategies for Spectroscopy: From Small Molecules to Nano Systems*; Barone, V., Ed.; Wiley: Chichester, U. K., 2011; pp 517–547.
- (33) Caruso, P.; Causà, M.; Cimino, P.; Crescenzi, O.; D'Amore, M.; Improta, R.; Pavone, M.; Rega, N. *Theor. Chem. Acc.* **2012**, *131*, 1211–1219.
- (34) Barone, V.; Bloino, J.; Monti, S.; Pedone, A.; Prampolini, G. *Phys. Chem. Chem. Phys.* **2010**, *12*, 10550–10561.
- (35) Barone, V.; Bloino, J.; Monti, S.; Pedone, A.; Prampolini, G. *Phys. Chem. Chem. Phys.* **2011**, *13*, 2160–2166.
- (36) Cascella, M.; Cuendet, M.; Tavernelli, I.; Rothlisberger, U. *J. Phys. Chem. B* **2007**, *111*, 10248–10252.

- (37) Demachy, I.; Ridard, J.; Laguitton-Pasquier, E.; Durnerin, G. V.; Archirel, P.; Lévi, B. *J. Phys. Chem. B* **2005**, *109*, 24121–24133.
- (38) Pedone, A.; Prampolini, G.; Monti, S.; Barone, V. *Phys. Chem. Chem. Phys.* **2011**, *13*, 16689–16697.
- (39) Pedone, A.; Prampolini, G.; Monti, S.; Barone, V. *Chem. Mater.* **2011**, *23*, 5016–5023.
- (40) Biczysko, M.; Bloino, J.; Brancato, G.; Cacelli, I.; Cappelli, C.; Ferretti, A.; Lami, A.; Monti, S.; Pedone, A.; Prampolini, G.; Puzzarini, C.; Santoro, F.; Trani, F.; Villani, G. *Theor. Chem. Acc.* **2012**, *131*, 1201–1220.
- (41) Gonçalves, M. B.; Dreyer, J.; Lupieri, P.; Barrera-Patiño, C.; Ippoliti, E.; Webb, M. R.; Corrie, J. E. T.; Carloni, P. *Phys. Chem. Chem. Phys.* **2013**, *15*, 2177–2183.
- (42) Czar, M. F.; Jockusch, R. A. *ChemPhysChem.* **2013**, *14*, 1138–1148.
- (43) Lipparini, F.; Cappelli, C.; Scalmani, G.; De Mitri, N.; Barone, V. *J. Chem. Theory Comput.* **2012**, *8*, 4270–4278.
- (44) Lipparini, F.; Cappelli, C.; Barone, V. *J. Chem. Theory Comput.* **2012**, *8*, 4153–4165.
- (45) Steindal, A. H.; Ruud, K.; Frediani, L.; Aidas, K.; Kongsted, J. *J. Phys. Chem. B* **2011**, *115*, 3027–3037.
- (46) De Angelis, F.; Santoro, F.; Nazeruddin, M. K.; Barone, V. *J. Phys. Chem. B* **2008**, *112*, 13181–13183.
- (47) Tiberio, G.; Muccioli, L.; Berarardi, R.; Zannoni, C. *ChemPhysChem* **2010**, *11*, 1018–1028.
- (48) Rhee, Y. M. I. N. *Int. J. Quantum Chem.* **2011**, *111*, 4091–4105.
- (49) Pipolo, S.; Benassi, E.; Brancolini, G.; Valášek, M.; Mayor, M.; Corni, S. *Theor. Chem. Acc.* **2012**, *131*, 1274–1288.
- (50) Barone, V.; Cacelli, I.; De Mitri, N.; Licari, D.; Monti, S.; Prampolini, G. *Phys. Chem. Chem. Phys.* **2013**, *15*, 3736–3751.
- (51) Cacelli, I.; Prampolini, G. *J. Chem. Theory Comput.* **2007**, *3*, 1803–1817.
- (52) Cicogna, F.; Coiai, S.; Passaglia, E.; Tucci, I.; Ricci, L.; Ciardelli, F.; Batistini, A. *J. Polym. Sci. A* **2011**, *49*, 781–795.
- (53) Cicogna, F.; Coiai, S.; Pinzino, C.; Ciardelli, F.; Passaglia, E. *React. Funct. Polym.* **2012**, *72*, 695–702.
- (54) Monti, S.; Cicogna, F.; Passaglia, E.; Prampolini, G.; Barone, V. *Phys. Chem. Chem. Phys.* **2011**, *13*, 21471–21478.
- (55) Adamo, C.; Barone, V. *J. Chem. Phys.* **1999**, *110*, 6158–6170.
- (56) Barone, V.; Cimino, P.; Stendardo, E. *J. Chem. Theory Comput.* **2008**, *4*, 751–764.
- (57) Barone, V.; Cimino, P. *Chem. Phys. Lett.* **2008**, *454*, 139–143.
- (58) Frisch, M. J.; Trucks, G. W.; Schlegel, H. B.; Scuseria, G. E.; Robb, M. A.; Cheeseman, J. R.; Scalmani, G.; Barone, V.; Mennucci, B.; Petersson, G.; Nakatsuji, H.; Caricato, M.; Li, X.; Hratchian, H. P.; Izmaylov, A. F.; Bloino, J.; Zheng, G.; Sonnenberg, J. L.; Hada, M.; Ehara, M.; Toyota, K.; Fukuda, R.; Hasegawa, J.; Ishida, M.; Nakajima, T.; Honda, Y.; Kitao, O.; Nakai, H.; Vreven, T.; Montgomery, J. A.; Peralta, J. E.; Ogliaro, F.; Bearpark, M.; Heyd, J. J.; Brothers, E.; Kudin, K. N.; Staroverov, V. N.; Kobayashi, R.; Normand, J.; Raghavachari, K.; Rendell, A.; Burant, J.; Iyengar, S. S.; Tomasi, J.; Cossi, M.; Rega, N.; Millam, J. M.; Klene, M.; Knox, J. E.; Cross, J. B.; Bakken, V.; Adamo, C.; Jaramillo, J.; Gomperts, R.; Stratmann, R. E.; Yazyev, O.; Austin, A. J.; Cammi, R.; Pomelli, C.; Ochterski, J. W.; Martin, R. L.; Morokuma, K.; Zakrzewski, V. G.; Voth, G. A.; Salvador, P.; Dannenberg, J. J.; Dapprich, S.; Parandekar, P. V.; Mayhall, N. J.; Daniels, A. D.; Farkas, O.; Foresman, J. B.; Ortiz, J. V.; Cioslowski, J.; Fo, D. *J. Gaussian 09*, revision C.01; Gaussian, Inc.: Wallingford, CT, 2009.
- (59) Jorgensen, W.; Maxwell, D.; Tirado-Rives, J. *J. Am. Chem. Soc.* **1996**, *118*, 11225–11236.
- (60) Damm, W.; Frontera, A.; Tirado-Rives, J.; Jorgensen, W. *J. Comput. Chem.* **1997**, *18*, 1955–1970.
- (61) Marenich, A.; Jerome, S.; Cramer, C.; Truhlar, D. *J. Chem. Theory Comput.* **2012**, *8*, 575–584.
- (62) van der Spoel, D.; Lindahl, E.; Hess, B.; van Buuren, A. R.; Apol, E.; Meulenhoff, P.; Tieleman, D.; Sijbers, A.; Feenstra, K.; van Drunen, R.; Berendsen, H. *GROMACS4.5, Gromacs User Manual version 4.5.4*. [www.gromacs.org](http://www.gromacs.org).
- (63) Berendsen, H. J. C.; Postma, J. P. M.; van Gunsteren, W.; Di Nola, A.; Haak, J. R. *J. Chem. Phys.* **1984**, *81*, 3684–3690.